Asymmetric Proton-Exchange-Enhanced Lithium Niobate and Silicon Low-Temperature Direct Bonding with Ultrathin Heterogeneous Interface

Yu Du[a,b], Yuanshu Zou[a], Bingxuan Zhu[c], Heng Jiang[b], Yao Chai[b], Chi Chung Tsoi[b], Xuming Zhang[b,*], Chenxi Wang[a,*]

[a] *State Key Laboratory of Precision Welding & Joining of Materials and Structures, Harbin Institute of Technology, Harbin 150001, China*

[b] *Photonics Research Institute, Department of Applied Physics, The Hong Kong Polytechnic University, Hong Kong, China*

[c] *Sauvage Laboratory for Smart Materials, School of Materials Science and Engineering, Harbin Institute of Technology (Shenzhen), Shenzhen 518055, China*

* Corresponding authors: wangchenxi@hit.edu.cn *(C.X. Wang) and* apzhang@polyu.edu.hk *(X.M. Zhang)*

Abstract:

The integration of lithium niobate ($LiNbO_3$, or LN) and silicon (Si) has emerged as a promising heterogeneous platform for micro-electromechanical systems (MEMS) and photonic integrated circuits (PICs). Particularly, the lithium niobate on silicon (LNOS) architecture leverages the superior piezo-optomechanical properties of LN, making it compatible with superconducting circuits and quantum systems. This opens an avenue for the development of advanced quantum sensors and processors. However, existing LN and Si bonding methods suffer from inherent limitations, such as low interfacial strength and the formation of thick, amorphous interlayers. In this work, we present an asymmetric surface activation strategy to address these challenges. By employing proton-exchange-enhanced chemical activation on the LN surface and oxygen plasma treatment on the Si side, we have achieved remarkable bonding strengths up to 10 MPa at a moderate annealing temperature of 150°C. Notably, the bonding mechanism in our approach differs from conventional diffusion-based processes. Here, the dehydration condensation of surface functional groups results in an exceptionally thin interfacial layer, less than 2 nm thick, without the presence of amorphous LN. This innovative fabrication method for LNOS demonstrates superior reliability, piezoelectric performance, thermal management capabilities, and optical transmission qualities, paving the way for cutting-edge photonic and quantum applications.

Keywords: lithium niobate; silicon; wafer bonding; waveguide; photonic integrated circuits

1. Introduction

Lithium niobate ($LiNbO_3$, or LN), which has been described as the "silicon of photonics", stands out as one of the most promising materials due to its unique combination of advantageous properties: (i) large electro-optic, piezoelectric, and nonlinear-optic material coefficient; (ii) broad transparency (400 nm to 5 μm); (iii) long-term stability; and (iv) widespread commercial availability of large, low-cost, optical-quality wafers[1]. What's more, the heterogeneous structure of lithium niobate and silicon (Si) offers more versatility and functionality, which has been utilized as microfluidic chips[2], photonic integrated circuits (PICs) [3–5], radio frequency (RF) devices[6,7], and quantum processors[8,9].

Wafer bonding is a premium heterogeneous integration method without considering lattice constants, especially for semiconductors or functional materials. Intermediate layers, such as Au[10,11] and Ag[12] for thermal compression bonding or benzocyclobutene (BCB)[13,14], ultraviolet (UV) glue[15], and polyimide (PI)[16] for adhesive bonding, are widely used to bond LN and Si. While this method is convenient, it introduces a new interface with distinct mechanical, optical, and electrical properties engendering a more intricate system[17]. Moreover, the organic adhesives are prone to aging and degradation[18]. Direct wafer bonding (chemical activated bonding, or DWB), a more promising method, employs strong oxidizing chemicals to activate the material and high temperature annealing to create a robust bond through a chemical reaction between functional groups on the surface. Chemical activation is facile and does not introduce harsh damage to the material. Ammonia peroxide mixture (APM)[19] has been used to bond LN and Si with only a 2 nm amorphous layer at the interface. Typically, high-temperature annealing is necessary to initiate the bonding reaction for sufficient strength and repair the damage to the interface. Unfortunately, due to the large mismatch in the coefficient of thermal expansion (CTE) between LN ($7.5\sim14.4 \times 10^{-6}$ m·K^{-1}, depending on cutting orientation) and Si (2.6×10^{-6} m·K^{-1}), thermal mismatch-induced stress at the interface during heating and cooling will result in

bonding failure[20]. Therefore, the LN and Si direct bonding was trapped in a dilemma.

The wafer bonding process is an exothermic reaction, the Gibbs free energy of the initial separated state $G_{LN} + G_{Si}$ is higher compared with the final bonded state $G_{LN/Si}$. The wafer bonding reaction can only be triggered by adding energy to the initial system to ensure that ($G_{LN} + G_{Si}$) + E_A is exceeded, where E_A is the activation energy. A schematic view is given in Figure 1a. Based on this theory, significant efforts have been devoted to realizing low-temperature LN and Si direct bonding. One straightforward approach is to increase the bonding temperature. Laser irradiation was used to locally heat to improve the bonding strength, avoiding the limitation of annealing temperature. A bond strength of over 2 MPa was obtained, but the 50 nm bonding interface might be detrimental to device performance[21,22]. Another way is to reduce the activation energy (E_A) required for the bonding reaction. Surface-activated bonding (SAB) employs the argon atom beam or ion beam to bombard the material surface transforming the single crystals into amorphous structures and bonding two unstable wafers together in an ultrahigh vacuum. By this method, LN and Si realized the average bonding strength of 9.8 MPa[23]. However, SAB has several drawbacks: (i) ultrahigh vacuum environment and a notably uncommon vacuum chamber configuration make this route both impractical and prohibitively expensive[24]; (ii) the 6 nm amorphous bonding interface can degrade the material structure and characteristics[25], especially the piezoelectric and nonlinear optical properties of LN[26–28]; (iii) argon irradiation can introduce homogeneous polarization in LN[29], affecting the function and reliability of the device. To address these challenges, plasma-activated bonding (PAB) has been proposed. This technique uses more moderate plasma, which not only physically activates the surface (reduce the activation energy (E_A)) to speed up diffusion bonding but also chemically introduces functional groups (generate a temporary state with increased Gibbs free energy ($G_{LN}^{*}+G_{Si}^{*}$)) for bonding reaction. Various plasma, oxygen (O_2), nitrogen (N_2), and Argon (Ar) plasma, have been explored for LN and Si direct bonding[30–32]. Oxygen plasma can prevent the

out-diffusion of oxygen atoms from the LN substrate[33] and realize higher bonding strength of 2.5 MPa[34]. To further improve the bonding strength, Xu[35] proposed a sequential plasma strategy including oxygen plasma with water vapor and nitrogen plasma to establish high-density and multiple functional groups for adequate bonding reaction, resulting in 3.2 MPa bonding strength and a 6.4 nm bonding interface. Despite these advancements, achieving high-quality LN and Si bonding remains an ongoing challenge.

In this paper, we propose a novel asymmetric surface activation strategy to realize low-temperature and high-quality direct bonding of LN and Si. The poor bond performance of the LN/Si bonding pair is attributed to the chemical stability of LN. Consequently, a two-step chemical activation was conducted on the LN side. First, proton exchange was used to eliminate the inertness of LN, followed by APM activation, which activated the LN without damaging its crystal structure. On the Si side, standard and efficient oxygen plasma activation was utilized. As a result, the highest bond strength of 10 MPa was achieved at 150℃ annealing. Bonding interface characterization revealed that the bonding mechanism involves the dehydration condensation of hydroxyl groups (-OH) on the surface, rather than traditional diffusion bonding. Therefore, this asymmetric approach resulted in an ultrathin bonding interface of less than 2 nm and preserved the pristine properties of LN with no crystal damage. A comparison about LN and Si direct bonding between this work and the previously reported methods is summarized in Table 1. This bonding strategy overcomes the bad bondability of LN and paves the way for LN micro-electromechanical systems (MEMS) and ultra-low loss quantum photonic lithium niobate on silicon (LNOS) platforms.

2. Material and methods

2.1 Bonding specimens

Experiments were performed on 500-μm-thick, 10×10 mm, X-cut lithium niobate and 500-um-thick, 10×10 mm, (100)-oriented n-type silicon, both polished on two sides. Wafer bonding

is not only related to material properties but also influenced by structural mechanics. While the influence of substrate thickness on bonding has been studied[36], this work primarily focused on optimizing surface activation methods. Therefore, the experiments were carried out using substrates of similar sizes as previous work[35], which is convenient for comparison, and the developed bonding method is compatible with various reported Si-LN configurations[37–39]. Proton exchange was carried out using 98% sulfuric acid. 28%~30% ammonium hydroxide solution, 35% hydrogen peroxide solution, and deionized water (DI water) were used for chemical activation. The inductively coupled plasma reactive ion etcher (ICP-RIE, Trion Phantom III) was utilized to provide oxygen (O_2) plasma for plasma activation. Before the experiments, LN chips were ultrasonically cleaned sequentially with acetone, isopropyl alcohol (IPA), and DI water. Si chips were given a bath in RCA1 solution (NH_4OH: H_2O_2: H_2O = 1:1:5) at 80°C for 10 minutes to remove organic impurities and particles.

2.2 Bonding procedures

In this experiment, an asymmetric surface activation method was employed to bond LN and Si, as depicted in Figure 1b.

Towards the LN side, a two-step chemical activation process was conducted based on previous work[40]. First, proton exchange (PE) in sulfuric acid was performed at 120℃ for varying durations to explore the influence of low-temperature sulfuric acid PE on LN. After PE, APM (NH_4OH: H_2O_2: H_2O = 1:2:7) was utilized to chemically activate LN at 80℃. Then, nitrogen flow was employed to dry the chips.

On the Si side, oxygen plasma activation was used, which has been verified effective for Si wafer bonding[41]. Cleaned Si chips were placed in the ICP-RIE chamber and exposed to oxygen plasma for 1 minute. In this experiment, strong etching will introduce a rough surface and be harmful to bonding quality. In this case, the plasma parameters were optimized according to the influence of the surface roughness, which is shown in Figure S1. As a result, the plasma

power was 600 W, the bias power was 100 W, the gas flow rate and pressure of the chamber were 100 sccm and 50 mTorr, respectively.

After the chemical activation of LN and plasma activation of Si, two chips were bonded together and annealed at 150℃ for 24 hours in an atmosphere environment, the annealing curve is depicted in Figure 1c. Comparison tests were conducted at identical temperatures to demonstrate the effectiveness of the PE-enhanced activation bonding method.

2.3 Characterization methods

The hydrogen element and depth of PE were measured by time-of-light secondary ion mass spectroscopy (TOF-SIMS, ION-TOF GmbH). The crystal composition of LN treated by PE for different periods was characterized utilizing Raman spectroscopy (Metatest ScanPro Advance). The element contents and surface chemical states were analyzed using X-ray photoelectron spectroscopy (XPS, Thermo Fisher Nexsa). The surface crystal structure was characterized by Grazing incidence X-ray diffraction (GIXRD, Panalytical Empyrean) with an incident angle of 1°. The influence of different treatments on the surface roughness, morphology, and piezoelectricity of the samples was investigated using atomic force microscopy (AFM, Bruker Dimension Fastscan) and piezoresponse force microscopy (PFM). In addition, transmission electron microscopy (TEM, Talos F200X G2) was used to characterize the bonding interface, and energy dispersive X-ray spectroscopy (EDX) mapping was used to characterize the elemental distributions.

To assess the bonding strength, a tensile test was conducted[42]. Firstly, the bonding pairs were glued to the steel blocks using an epoxy adhesive. Then, the bonded sample was assembled onto a tensile tester (Shimadzu AG-20kNX) and subjected to pulling apart at a rate of 0.2 mm/min. The actual tensile force measured at the point of sample separation divided by the bonding area was taken as the bonding strength.

2.4 Simulation methods

To verify the effect of proton exchange, theoretical calculations based on the first-principles calculations density functional theory (DFT) and *ab initio* molecular dynamics (MD) were used to study the adsorption of water molecules on pristine and proton-exchanged LN[43]. All the calculations were carried out using the Vienna *ab initio* simulation package[44,45] with a cutoff energy of 500 eV and a generalized gradient approximation with the Perdew−Burke−Ernzerh of parametrization[46]. Software VESTA[47] was used for all atomistic visualizations.

The performance of LNOS was simulated to demonstrate the superiority of the ultrathin bonding interface. To simulate the thermal management in electro-optic modulators, the waveguide temperature was calculated under different power of the electrodes by COMSOL 6.0. The optical transmission loss of different LN optical platforms was simulated with a finite-difference frequency-domain (FDTD) mode solver program by Lumerical MODE solutions software.

3. Results and discussion

3.1 Characterization and optimization of low-temperature proton exchange

Previously, PE for LN was employed to fabricate optical waveguides confining light to the micrometer range, so a high temperature above 200℃ was necessary to improve the efficiency of PE for a significant depth[48,49]. However, in this experiment, PE was considered as a surface treatment method, in which the depth is not meaningful. The key to this treatment is to ensure the effect of surface preparation and avoid damage to LN. Therefore, PE used sulfuric acid at a low temperature of 120℃ referencing to the temperature of sulfuric peroxide mixture (SPM), a conventional standard clean method. This low-temperature PE was firstly performed on LN, so the effect of PE was verified by SIMS, which has proven to be a useful technique for performing depth profiling studies. Elemental composition information of the LN sample after 2-hour PE was derived through SIMS and the spectrum is presented in Figure 2a. The relatively

constant O profiles are consistent with the fact that the exchange is primarily between Li and H. In region I close to the sample surface, the H concentration is slightly low due to the storage from PE to characterization. Subsequently, the H concentration stabilizes into a steplike region II extending from ~50 nm to 170 nm deep. Finally, the profile makes the transition gradually into the substrate in the region III, where the H concentration drops to 50% of its concentration value about 184 nm. According to this, the diffusion coefficient of the protons $D_a(T)$ is calculated to be 4.2×10^{-3} μm^2h^{-1}, where T = 120°C. The diffusion curve about diffusion depth d_a and time t is inserted in Figure 2a, as described in equation (1)[50]. Hence, the diffusion depth can be controlled according to PE time. Additionally, proton exchanged lithium niobate (PELN) showed a higher etching rate of 4 nm/min compared to pristine LN, which had an etching rate of 1.27 nm/min by argon plasma.

$$d_a(T,t) = 2[D_a(T)t]^{1/2} \qquad (1)$$

To complete compositional characterization, surface XPS measurements were performed at the surface region of pristine and PELN. The XPS spectra of the core-level Li1s and Nb4s are shown in Figure 2b. The content of Li decreased from the original 12.4% to 2.1% after a 5-minute PE, in contrast, the Nb element showed no difference. What's more, no changes in chemical shift were observed, indicating that Li retains Li_2O (55 eV)[31,51] structure during the PE process. Raman scattering has been reported to characterize the stoichiometry of LN[52]. In this experiment, all Raman scattering tests were conducted at room temperature for pristine LN and PELN. The shape of the E-phonon at 153 cm^{-1}, measurable in the configurations Z(YZ)X, is inserted in Figure 2c, which showed an almost symmetrical broadening and decreasing intensity with a prolonged PE time. What's more, the content of Li can be calculated according to equation (2)[52,53], in which c_{Li} is the Li content of the crystal and Γ is the halfwidth of the Raman lines at 153 cm^{-1}. The curve is depicted in Figure 2c, further verifying that the Li is replaced by H during the PE process.

$$c_{Li}[mol\%] = 53.03 - 0.4739\Gamma[cm^{-1}] \quad (2)$$

FTIR identifies chemical bonds in a molecule by producing an infrared absorption spectrum, especially sensitive to hydrogen bonds. The O-H stretching region of pristine LN and different time PELN are characterized by FTIR in attenuated total reflection (ATR) mode, as shown in Figure 2d. The unexchanged LN showed two closely spaced bands, a strong band at 3485 cm^{-1} and a shoulder indicating the presence of a weaker band at approximately 3470 cm^{-1}. As the proton dose increased, a new band at 3450 cm^{-1} became stronger, in agreement with previous reports[54,55].

The impact of PE on surface topography was investigated using AFM. The Ra value and the 3D morphology are shown in Figure 2e and 2f, respectively. The mean Ra value of the pristine LN is 0.31 nm. Extended PE resulted in increased roughness, with the roughness exceeding 0.4 nm after a 25-minute PE. Surface topography plays a prominent role in improving bonding area and increasing bonding energy. Therefore, shorter PE time is a good choice. Additionally, the GIXRD was employed to detect the influence of PE on the surface crystal quality. The full spectra are shown in Figure S2 and enlarged characteristic peak spectra are shown in Figure 2g. The single crystal will show no diffraction peaks, as shown in the pristine LN. After PE treatment, a new diffraction peak appeared at about 2θ = 49°, indicating surface crystal damage and a trend toward amorphization. What's more, the intensity of the diffraction peak increased with prolonged PE time. The crystal damage is detrimental to the piezoelectrical and electro-optical properties of LN. However, annealing can help repair the crystal structure[28]. For LN samples subjected to 3-minute and 5-minute PE, the diffraction peak disappeared after annealing, in accordance with the curve in Figure 1c. Notably, the effect of repairment is limited and cannot fully recover the crystal structure for the LN sample experiencing a 10-minute PE. Based on the above characterization, the surface of LN can be effectively proton exchanged

within a 10-minute treatment, and the physical damage to LN requires a shorter PE treatment. Consequently, a 5-minute PE was used for the subsequent chemical activation of LN.

3.2 Effect and mechanism of proton exchange-enhanced surface activation

To demonstrate the effect of PE pretreatment on bonding performance, a comparative test was conducted. LN, with and without PE, were activated by a short 5-minute APM and then bonded to oxygen plasma-activated Si. As shown in Figure 3a, the two-step treatment involving PE pretreatment significantly enhanced the bonding strength to 7.95 MPa, compared to 1.39 MPa for LN activated only by APM, indicating the substantial effect of PE pretreatment. Further experiments explored the impact of varying APM activation times. According to our previous work[40], APM has a stronger etching effect on PELN compared to pristine LN and prolonged APM activation can easily etch away the thin PE surface. Consequently, in this experiment, when APM activation reached 10 minutes, LN with PE pretreatment showed almost the same bonding strength as LN without PE pretreatment due to the removal of the thin PELN layer.

The surface topography was characterized by AFM for APM-activated LN samples with and without PE. The Ra value is shown in Figure 3b, and 3D morphology is shown in Figure S3. Due to the etching effect, LN without PE showed an increase of roughness but remained within 0.37nm to 0.38nm during the prolonged APM process, indicating the chemical stability of LN. In contrast, the surface roughness of PELN exhibited a significant increase from 0.34 nm to 0.42 nm after 5-minute APM, which means the PE removes the chemical stability of LN and introduces a stronger etching effect. When the APM duration was longer than 5 minutes, the roughness slightly increased but was not very sensitive to the APM time, further demonstrating the disappearance of PELN layer.

The surface chemical state was characterized by XPS to explore the mechanism of PE-enhanced surface activation. Hydroxy groups (-OH) are crucial for hydrophilic bonding reactions. The contents of hydroxy groups on the LN surface and the core-level O1s with

different treatments are shown in Figure 3c and 3d. APM or PE increased the oxygen content above 40% because of the strong chemical oxidation. However, the content of hydroxy groups showed no improvement after APM due to the chemical stability of LN, which explains the weak bonding strength. PE pretreatment introduced 23.5% hydroxy groups from the original 16.9% and following APM further improved the content to 25.6%. According to the analysis of bonding strength and surface morphology, two-step treatment introduced a rougher surface but resulted in higher strength, attributed to more hydroxy groups on the surface for bonding reactions. What's more, Figure S4 presents the XPS spectra of the core-level Nb3d and C1s. Proton exchange showed no influence on the Nb element. The content of carbon decreased after APM, which can remove the organic contamination from the surface through chemical reaction and etching.

Theoretical calculations based on the DFT-MD were used to study the adsorption of water molecules on the surface of pristine and proton exchanged LN, as shown in Figure 3e. The elementary structures of LN slabs with and without proton exchange in the simulation are shown in Figure S5. LN showed different chemical reactivities after PE. Water molecules are more easily adsorbed on the surface and create bonds with LN compared to pristine LN. What's more, the mean adsorption energy of water molecules increased to -0.95 eV after PE from the original -0.75eV. Consequently, more water molecules can be adsorbed on the surface, resulting in more hydroxy groups for bonding reaction, consistent with the above XPS results.

3.3 Characterization and properties of ultrathin bonding interface

To observe the LN and Si bonding interface of this asymmetric activated bonding method, the cross-section (LN: 5-minute PE followed 5-minute APM; Si: O_2 plasma) at a bonding temperature of 150℃ was fabricated by the focus ion beam (FIB) and analyzed by TEM. The TEM sample and bright field (BF) image of the bonding interface are shown in Figure 4a and 4b, separately. The bonding interface was smooth and void-free, indicating that the bonding

pair can withstand the ion bombardment and the stress produced by the harsh mechanical and polishing process. Figure 4c shows a high-resolution transmission electron microscopy (HRTEM) image of the bonding pair, where the bonding interface was tight. Additionally, the lattice of the monocrystalline LN $(1\bar{1}0)$ and Si $(01\bar{1})$ crystal orientation was evident, as exhibited in the inserted selected area electron diffraction (SAED) images of Figure 4c.

Figure 4d provides the scanning transmission electron microscopy (STEM) image and elemental distribution maps (red: Nb; green: O; blue: Si) in high-angle annular dark field (HAADF) mode. The boundary of the LN and Si interface was distinct. There was no diffusion of the Nb element because the chemical activation is a moderate treatment for the surface and does not introduce structural damage to promote diffusion for high bonding strength[56]. Therefore, the bonding mechanism of this method is only the dehydration condensation reaction, as shown in reaction (3), rather than the diffusion bonding in conventional PAB or SAB[25,51]. Notably, a transition layer composed of Si and O appeared on the right of the bonding interface, which was caused by the O_2 plasma activation and the reaction of Si and H_2O from reaction (3), as depicted in reaction (4)[41,57,58]. Finally, the surplus by-products, like water and hydrogen, can be exhausted through porous amorphous silicon dioxide (a-SiO_2)[57].

$$Nb - OH + Si - OH \rightarrow Nb - O - Si + H_2O \qquad (3)$$

$$2H_2O + Si \rightarrow SiO_2 + 2H_2 \qquad (4)$$

According to Figure 4c, the heterogeneous bonding interface can be divided into two sections, monocrystalline PELN and amorphous SiO_2. The SAED image of the bonding interface is shown in Figure 4e, which is composed of the diffraction spots of LN and Si crystal. This indicates that proton exchange did not change the crystal structure of LN. The HRTEM image of the LN side including PELN is exhibited in Figure 4f. The PELN area shows the same atomic arrangement and crystal structure as pristine LN. Geometrical phase analysis (GPA) was used to investigate the strain distribution by measuring the displacement of lattice fringes.

Figure 4g shows the uniform tensile (positive) strain on the LN and a compressive (negative) strain on the PELN because the lithium ion was replaced by the smaller hydrogen ion, resulting in crystal structure shrinkage from the original 2.64 Å to 2.6 Å, as the measurement results in Figure 4f. This slight structure shrinkage introduces a change of the refractive index, which has been widely used for LN optical waveguides and does not cause functional damage[49]. About the Si side, the HRTEM image and GPA analysis are shown in Figure 4h and 4i. There are some concentrations of tensile and compressive strain close to the bonding interface, but the strain distribution tends to decrease and become uniform when staying away from the interface.

The superiority of this ultrathin bonding interface was evaluated by a series of comparison tests from four aspects, including bonding reliability, piezoelectricity, thermal management, and optical waveguide performance. Firstly, the high bonding strength enables the heterogeneous structure to withstand harsh micro-nano processing and introduces high reliability to the fabricated devices. To demonstrate the superior performance of this asymmetric PE-enhanced surface activation bonding method, comparative experiments were conducted. When both LN and Si sides underwent the same APM treatment, the highest bonding strength was only 0.85 MPa, far from meeting the requirements of micro-nano fabrication. The O_2 plasma-activated bonding method was used to bond LN and Si, which showed a significant effect and reached 4.73 MPa. The highest tensile curves of both methods are shown in Figure 5a. To avoid the damage of plasma to the crystal structure of LN, an asymmetrical bonding method was employed, and the results are depicted in Figure 5b. The LN side was activated by APM, which does not introduce amorphous LN, and the Si side was activated by O_2 plasma for good bonding performance. This asymmetrical activated strategy was helpful to improve bonding strength to 2.75 MPa. Towards this method, LN without amorphous structure cannot realize high strength by diffusing with Si and the chemical stability of LN leads to less functional groups for bonding reaction. Therefore, the bonding strength is limited. When proton exchange was used to

eliminate the chemical inertness of LN, sufficient bonding reaction achieved 10 MPa bonding strength, which especially can meet the harsh MEMS fabrication[59].

To confirm the ferroelectric nature of LN after different treatments, local piezoelectrical properties were studied using PFM measurements at room temperature with an applied voltage of ± 8 V on the same capacitors. Compared with plasma activated LN sample in Figure 5c, the chemical-activated LN sample generated a well-defined phase loop and piezoelectric amplitude butterfly-like loop, as shown in Figure 5d. This indicates that LN subjected to chemical activation exhibits better ferroelectricity and polarization switching behavior, which are crucial for efficient piezo-optomechanical transduction[5,60].

The heterogeneous structures of LN have been widely used in PICs, like lithium niobate on insulator (LNOI) and LNOS integrated optics platforms. LNOI is a three-layer structure consisting of LN waveguide, SiO_2 insulator, and Si substrate. LNOS is a two-layer structure composed of an LN waveguide and Si substrate. Because the refractive index of Si is larger than the LN, undercutting is used to limit the light in the LN waveguide. In previous methods, PAB or SAB will introduce the amorphous LN between LN and Si. The bonding strategy proposed in this work has an ultrathin bonding interface and no damage to LN. The thermal performance and optical transmission loss were simulated according to the parameters in Table S1 and the structures in Figure S6 and S7. The parameters used When LN was used as an electro-optic modulator, the electrodes would heat and change the temperature of the waveguide to further influence the modulating effect[61]. The relationship between waveguide temperature and electrode heat power is shown in Figure 5e. Thanks to the low thermal conductivity of SiO_2, the heat is difficult to transfer to waveguide from electrodes and LNOI structure shows the lowest waveguide temperature. LNOS in this work shows better thermal performance compared to the conventional method, because of the low thermal conductivity of amorphous LN[62].

Therefore, this bonding strategy improves the thermal performance and stability of the devices based on LNOS.

Figure 5f provides the relationship between the radius and the optical transmission loss in a 90° bend using FDTD. The LNOI needs a radius larger than 20 μm, but LNOS can realize the lowest loss at a radius of 15 μm, indicating the LNOS is a more compact optical platform for PICs. The bend losses are dominant in the small radii region and the propagation losses are dominant in the large radii region. Therefore, the transmission loss exhibits a trend of first reducing and then increasing. Previous LNOS has lower radiation loss compared to LNOS in this work because amorphous LN has a lower refractive index[63], which can help limit the light. However, amorphous LN introduces optical absorption resulting in higher propagation loss, as shown in the figure inserted in Figure 5f. Therefore, LNOS produced by this bonding method can further reduce the optical transmission loss, which is necessary for superconducting quantum applications[8,28].

4. Conclusions

This paper introduces an asymmetric proton exchange-enhanced surface-activated bonding method to achieve LN and Si bonding with high bonding strength and ultrathin interface at a low temperature. Through characterization and theoretical simulation, the impact of proton exchange on the surface, including surface roughness, surface energy, crystal structure, and chemical state, was investigated. Tensile tests were conducted to evaluate the proposed asymmetric bonding method. Cross-sectional TEM analysis revealed a perfect bonding interface of less than 2 nm at 150℃ annealing. The mechanism of achieving a significant improvement by this bonding strategy is proton exchange eliminates the inertness of LN facilitating surface activation to yield high-density functional groups, then dehydration condensation realizes the high-strength and no-defect bonding. Furthermore, LNOS by this method holds superior piezoelectricity, thermal performance, and low optical loss. This study

lays a foundation for the development of LN-based MEMS and PICs.

Associated content

Supporting Information

The optimization of plasma activation parameters, GIXRD characterization of $LiNbO_3$ after proton exchange and annealing, morphology analysis of $LiNbO_3$ post-treatments, XPS analysis of carbon and niobium elements after various activation methods, and detailed simulations of surface adsorption and interface performance.

Author information

Corresponding authors

Chenxi Wang - *State Key Laboratory of Precision Welding & Joining of Materials and Structures, Harbin Institute of Technology, Harbin 150001, China;* Email: wangchenxi@hit.edu.cn

Xuming Zhang - *Photonics Research Institute, Department of Applied Physics, The Hong Kong Polytechnic University, Hong Kong, China;* Email: apzhang@polyu.edu.hk

Authors

Yu Du - *State Key Laboratory of Precision Welding & Joining of Materials and Structures, Harbin Institute of Technology, Harbin 150001, China; Photonics Research Institute, Department of Applied Physics, The Hong Kong Polytechnic University, Hong Kong, China*

Yuanshu Zou - *State Key Laboratory of Precision Welding & Joining of Materials and Structures, Harbin Institute of Technology, Harbin 150001, China*

Bingxuan Zhu - *Sauvage Laboratory for Smart Materials, School of Materials Science and Engineering, Harbin Institute of Technology (Shenzhen), Shenzhen 518055, China*

Heng Jiang - *Photonics Research Institute, Department of Applied Physics, The Hong Kong Polytechnic University, Hong Kong, China*

Yao Chai - *Photonics Research Institute, Department of Applied Physics, The Hong Kong*

Polytechnic University, Hong Kong, China

Chi Chung Tsoi - *Photonics Research Institute, Department of Applied Physics, The Hong Kong Polytechnic University, Hong Kong, China*

Author contributions

Y.D. conceived this work and performed the bonding experiments. Y.-S.Z., B.-X.Z., and H.J. analyzed the experiment data. Y.C. and C.-C.T. performed device simulations. X.-M.Z. and C.-X.W. designed and directed this project. Y.D., X.-M.Z., and C.-X.W. co-wrote the manuscript. All the authors discussed and commented on the manuscript.

Notes

The authors declare that they have no known competing financial interests or personal relationships that could have appeared to influence the work reported in this paper.

Acknowledgements

This work was supported by the National Natural Science Foundation of China (Grant Nos. 92164105 and 51975151), the Heilongjiang Provincial Natural Science Foundation of China under grant LH2019E041, the Heilongjiang Touyan Innovation Team Program (HITTY-20190013), The Hong Kong Polytechnic University (1-YY5V, 1-CD4V, 1-CD6U, G-SB6C, 1-CD8U, 1-BBEN, 1-W28S, 1-CD9Q, 1-SBVB, 1-CDJW, 1-CDJ8 and 1-W32A) and the Research Grants Council (RGC) of Hong Kong (15215620, N_PolyU511/20).

References

(1) Boes, A.; Chang, L.; Langrock, C.; Yu, M.; Zhang, M.; Lin, Q.; Lončar, M.; Fejer, M.; Bowers, J.; Mitchell, A. Lithium Niobate Photonics: Unlocking the Electromagnetic Spectrum. *Science* **2023**, *379* (6627), eabj4396. DOI: 10.1126/science.abj4396

(2) Wilson, R.; Reboud, J.; Bourquin, Y.; Neale, S. L.; Zhang, Y.; Cooper, J. M. Phononic Crystal Structures for Acoustically Driven Microfluidic Manipulations. *Lab Chip* **2011**, *11* (2), 323–328. DOI: 10.1039/c0lc00234h

(3) Chiles, J.; Fathpour, S. Mid-Infrared Integrated Waveguide Modulators Based on Silicon-on-Lithium-Niobate Photonics. *Optica* **2014**, *1* (5), 350. DOI: 10.1364/optica.1.000350

(4) Jiang, W.; Patel, R. N.; Mayor, F. M.; McKenna, T. P.; Arrangoiz-Arriola, P.; Sarabalis, C. J.; Witmer, J. D.; Van Laer, R.; Safavi-Naeini, A. H. Lithium Niobate Piezo-Optomechanical Crystals. *Optica* **2019**, *6* (7), 845. DOI: 10.1364/optica.6.000845

(5) Jiang, W.; Sarabalis, C. J.; Dahmani, Y. D.; Patel, R. N.; Mayor, F. M.; McKenna, T. P.; Van Laer, R.; Safavi-Naeini, A. H. Efficient Bidirectional Piezo-Optomechanical Transduction between Microwave and Optical Frequency. *Nat Commun* **2020**, *11* (1), 1166. DOI: 10.1038/s41467-020-14863-3

(6) Mandal, S.; Arts, K.; Morgan, D. J.; Chen, Z.; Williams, O. A. Zeta Potential and Nanodiamond Self Assembly Assisted Diamond Growth on Lithium Niobate and Lithium Tantalate Single Crystal. *Carbon* **2023**, *212*, 118160. DOI: 10.1016/j.carbon.2023.118160

(7) Ghosh, S. Acoustic Wave Amplification with Thin Film Silicon Bonded on Lithium Niobate. *Journal of Micromechanics and Microengineering* **2022**, *32* (11), 114001. DOI: 10.1088/1361-6439/ac9289

(8) Arrangoiz-Arriola, P.; Wollack, E. A.; Pechal, M.; Witmer, J. D.; Hill, J. T.; Safavi-Naeini, A. H. Coupling a Superconducting Quantum Circuit to a Phononic Crystal Defect Cavity. *Phys Rev X* **2018**, *8* (3), 031007. DOI: 10.1103/PHYSREVX.8.031007

(9) Arrangoiz-Arriola, P.; Wollack, E. A.; Wang, Z.; Pechal, M.; Jiang, W.; McKenna, T. P.; Witmer, J. D.; Van Laer, R.; Safavi-Naeini, A. H. Resolving the Energy Levels of a Nanomechanical Oscillator. *Nature* **2019**, *571* (7766), 537–540. DOI: 10.1038/s41586-019-1386-x

(10) Clementi, G.; Ouhabaz, M.; Margueron, S.; Suarez, M. A.; Bassignot, F.; Gauthier-Manuel, L.; Belharet, D.; Dulmet, B.; Bartasyte, A. Highly Coupled and Low Frequency Vibrational Energy Harvester Using Lithium Niobate on Silicon. *Appl Phys Lett* **2021**, *119* (1), 013904. DOI: 10.1063/5.0052615

(11) Takigawa, R.; Higurashi, E.; Suga, T.; Kawanishi, T. Room-Temperature Transfer Bonding of Lithium Niobate Thin Film on Micromachined Silicon Substrate with Au Microbumps. *Sens Actuators A Phys* **2017**, *264*, 274–281. DOI: 10.1016/j.sna.2017.08.015

(12) Diest, K.; Archer, M. J.; Dionne, J. A.; Park, Y. B.; Czubakowski, M. J.; Atwater, H. A. Silver Diffusion Bonding and Layer Transfer of Lithium Niobate to Silicon. *Appl Phys Lett* **2008**, *93* (9), 092906. DOI: 10.1063/1.2976560

(13) Bai, X.; Shuai, Y.; Gong, C.; Wu, C.; Luo, W.; Böttger, R.; Zhou, S.; Zhang, W. Surface

Modifications of Crystal-Ion-Sliced $LiNbO_3$ Thin Films by Low Energy Ion Irradiations. *Appl Surf Sci* **2018**, *434*, 669–673. DOI: 10.1016/j.apsusc.2017.10.184

(14) Chen, L.; Reano, R. M. Compact Electric Field Sensors Based on Indirect Bonding of Lithium Niobate to Silicon Microrings. *Optics Express* **2012**, *20* (4), 4032–4038. DOI: 10.1364/OE.20.004032

(15) Mercante, A. J.; Yao, P.; Shi, S.; Schneider, G.; Murakowski, J.; Prather, D. W. 110 GHz CMOS Compatible Thin Film $LiNbO_3$ Modulator on Silicon. *Opt Express* **2016**, *24* (14), 15590. DOI: 10.1364/oe.24.015590

(16) Xue, G.; Geng, W.; Fu, W.; He, J.; Zhao, C.; Bi, K.; Qiao, X.; Wei, H.; Shi, Y.; Chou, X. Integrated Fabrication and Ferroelectric Domain Adjustment of Lithium Niobate Single Crystal Films Based on Silicon Substrate. *Mater Des* **2022**, *215*, 110447. DOI: 10.1016/j.matdes.2022.110447

(17) Du, Y.; Liu, L.; Zhu, B.; Jiang, H.; Zhang, X.; Wang, C. Low-Temperature Fusion Bonding of Aluminosilicate Glass via Intermediate Water. *Ceram Int* **2024**, *50* (7), 10252–10258. DOI: 10.1016/j.ceramint.2023.12.335

(18) Uddin, M. A.; Chan, H. P. The Challenges in the Fabrication of Reliable Polymer Photonic Devices. *Journal of Materials Science: Materials in Electronics* **2009**, *20*, 277-281. DOI: 10.1007/s10854-008-9581-9

(19) Namba, A.; Sugimoto, M.; Ogura, T.; Tomita, Y.; Eda, K. Direct Bonding of Piezoelectric Crystal onto Silicon. *Appl Phys Lett* **1995**, *67* (22), 3275–3276. DOI: 10.1063/1.114896

(20) Park, Y. B.; Min, B.; Vahala, K. J.; Atwater, H. A. Integration of Single-Crystal $LiNbO_3$ Thin Film on Silicon by Laser Irradiation and Ion Implantation-Induced Layer Transfer. *Advanced Materials* **2006**, *18* (12), 1533–1536. DOI: 10.1002/adma.200502364

(21) Kawano, H.; Takigawa, R.; Ikenoue, H.; Asano, T. Bonding of Lithium Niobate to Silicon in Ambient Air Using Laser Irradiation. *Japanese Journal of Applied Physics* **2016**, *55* (8S3), 08RB09. DOI: 10.7567/JJAP.55.08RB09

(22) Takigawa, R.; Kawano, H.; Ikenoue, H.; Asano, T. Investigation of the Interface between $LiNbO_3$ and Si Wafers Bonded by Laser Irradiation. *Jpn J Appl Phys* **2017**, *56* (8), 088002. DOI: 10.7567/JJAP.56.088002

(23) Takagi, H.; Maeda, R.; Suga, T. Room-Temperature Wafer Bonding of Silicon and Lithium Niobate by Means of Argon-Beam Surface Activation. *Integrated Ferroelectrics* **2002**, *50*, 53–59. DOI: 10.1080/10584580215523

(24) Miansari, M.; Friend, J. R. Acoustic Nanofluidics via Room-Temperature Lithium Niobate Bonding: A Platform for Actuation and Manipulation of Nanoconfined Fluids and Particles. *Adv Funct Mater* **2016**, *26* (43), 7861–7872. DOI: 10.1002/adfm.201602425

(25) Takagi, H.; Maeda, R.; Hosoda, N.; Suga, T. Room-Temperature Bonding of Lithium Niobate and Silicon Wafers by Argon-Beam Surface Activation. *Appl Phys Lett* **1999**, *74* (16), 2387–2389. DOI: 10.1063/1.123860

(26) Zhao, Y.; Liu, W.; Bao, Y.; Yang, F.; Wang, X. Plasma-Activated GaAs/Si Wafer Bonding with High Mechanical Strength and Electrical Conductivity. *Mater Sci Semicond Process* **2022**, *143*,

106481. DOI: 10.1016/j.mssp.2022.106481

(27) Xu, J.; Wang, C.; Zhang, R.; Cheng, J.; Li, G.; Xiang, J.; Tian, Y. VUV/O_3 Activated Direct Heterogeneous Bonding towards High-Performance $LiNbO_3$-Based Optical Devices. *Appl Surf Sci* **2019**, *495*, 143576. DOI: 10.1016/j.apsusc.2019.143576

(28) Shams-Ansari, A.; Huang, G.; He, L.; Li, Z.; Holzgrafe, J.; Jankowski, M.; Churaev, M.; Kharel, P.; Cheng, R.; Zhu, D.; Sinclair, N.; Desiatov, B.; Zhang, M.; Kippenberg, T. J.; Lončar, M. Reduced Material Loss in Thin-Film Lithium Niobate Waveguides. *APL Photonics* **2022**, *7* (8), 081301. DOI: 10.1063/5.0095146

(29) Howlader, M. M. R.; Suga, T.; Kim, M. J. A Novel Bonding Method for Ionic Wafers. *IEEE Transactions on Advanced Packaging* **2007**, *30* (4), 598–604. DOI: 10.1109/TADVP.2007.906394

(30) Tulli, D.; Janner, D.; Pruneri, V. Room Temperature Direct Bonding of $LiNbO_3$ Crystal Layers and Its Application to High-Voltage Optical Sensing. *Journal of Micromechanics and Microengineering* **2011**, *21* (8), 085025. DOI: 10.1088/0960-1317/21/8/085025

(31) Huang, R.; Tang, M.; Kan, W.; Xu, H.; Wu, K.; Wang, Z.; Li, H. Single-Crystalline $LiNbO_3$ Integrated onto Si-Based Substrates via Ar Plasma-Activated Low-Temperature Direct Bonding. *J Phys D Appl Phys* **2024**, *57* (1), 015102. DOI: 10.1088/1361-6463/acff05

(32) Weigel, P. O.; Savanier, M.; Derose, C. T.; Pomerene, A. T.; Starbuck, A. L.; Lentine, A. L.; Stenger, V.; Mookherjea, S. Lightwave Circuits in Lithium Niobate through Hybrid Waveguides with Silicon Photonics. *Sci Rep* **2016**, *6* (1), 22301. DOI: 10.1038/srep22301

(33) Chiles, J.; Fathpour, S. Mid-Infrared Integrated Waveguide Modulators Based on Silicon-on-Lithium-Niobate Photonics. *Optica* **2014**, *1* (5), 350. DOI: 10.1364/optica.1.000350

(34) Wu, C. C.; Horng, R. H.; Wuu, D. S.; Chen, T. N.; Ho, S. S.; Ting, C. J.; Tsai, H. Y. Thinning Technology for Lithium Niobate Wafer by Surface Activated Bonding and Chemical Mechanical Polishing. *Japanese Journal of Applied Physics, Part 1: Regular Papers and Short Notes and Review Papers* **2006**, *45* (4 B), 3822–3827. DOI: 10.1143/JJAP.45.3822

(35) Xu, J.; Ren, Z.; Liu, X.; Xu, C.; Wang, C.; Tian, Y.; Lee, C. Heterogeneous $LiNbO_3$/Si Direct Bonding for Wavelength-Dependent Mid-Infrared Imaging. *2021 21st International Conference on Solid-State Sensors, Actuators and Microsystems (TRANSDUCERS)* **2021**, 585–588. DOI: 10.1109/Transducers50396.2021.9495511

(36) Prabhakar, K.; Patton, R. J.; Reano, R. M. Stress Reduction and Wafer Bow Accommodation for the Fabrication of Thin Film Lithium Niobate on Oxidized Silicon. *Journal of Vacuum Science & Technology B* **2021**, *39* (6), 62208. DOI: 10.1116/6.0001283

(37) Xu, S.; Liu, W.; Le, X.; Lee, C. Unveiling Efficient Acousto-Optic Modulation in Silicon Photonic Devices via Lithium Niobate Using Transfer Printing. *Nano Lett* **2024**, *24* (41), 12964–12972. DOI: 10.1021/acs.nanolett.4c03622

(38) Tan, Y.; Niu, S.; Billet, M.; Singh, N.; Niels, M.; Vanackere, T.; Van Kerrebrouck, J.; Roelkens, G.; Kuyken, B.; Van Thourhout, D. Micro-Transfer Printed Thin Film Lithium Niobate (TFLN)-on-Silicon Ring Modulator. *ACS Photonics* **2024**, *11* (5), 1920–1927. DOI: 10.1021/acsphotonics.3c01869

(39) Xu, S.; Ren, Z.; Dong, B.; Zhou, J.; Liu, W.; Lee, C. Mid-Infrared Silicon-on-Lithium-Niobate Electro-Optic Modulators Toward Integrated Spectroscopic Sensing Systems. *Adv Opt Mater* **2023**, *11* (4), 2202228. DOI: 10.1002/ADOM.202202228

(40) Du, Y.; Pang, Z.; Zou, Y.; Zhu, B.; Liu, L.; Zhang, X.; Wang, C. Proton Exchange-Enhanced Surface Activated Bonding for Facile Fabrication of Monolithic Lithium Niobate Microfluidic Chips. *Chemical Engineering Journal* **2024**, *496*, 154046. DOI: 10.1016/j.cej.2024.154046

(41) Plach, T.; Hingerl, K.; Stifter, D.; Dragoi, V.; Wimplinger, M. Investigations on Bond Strength Development of Plasma Activated Direct Wafer Bonding with Annealing. *ECS Trans* **2013**, *50* (7), 277–285. DOI: 10.1149/05007.0277ecst

(42) Kaaos, J.; Ross, G.; Paulasto-Kröckel, M. Aluminum Nitride to Silicon Direct Bonding for an Alternative Silicon-On-Insulator Platform. *ACS Appl Mater Interfaces* **2021**, *13* (32), 38857–38865. DOI: 10.1021/acsami.1c09535

(43) Zhang, D.; Peng, L.; Yi, P.; Lai, X. Electronic Transport and Corrosion Mechanisms of Graphite-Like Nanocrystalline Carbon Films Used on Metallic Bipolar Plates in Proton-Exchange Membrane Fuel Cells. *ACS Appl Mater Interfaces* **2021**, *13* (3), 3825–3835. DOI: 10.1021/acsami.0c17764

(44) Kresse, G.; Furthmüller, J. Efficiency of Ab-Initio Total Energy Calculations for Metals and Semiconductors Using a Plane-Wave Basis Set. *Comput Mater Sci* **1996**, *6* (1), 15–50. DOI: 10.1016/0927-0256(96)00008-0

(45) Kresse, G.; Furthmüller, J. Efficient Iterative Schemes for *Ab Initio* Total-Energy Calculations Using a Plane-Wave Basis Set. *Phys Rev B* **1996**, *54* (16), 11169. DOI: 10.1103/PhysRevB.54.11169

(46) Perdew, J. P.; Burke, K.; Ernzerhof, M. Generalized Gradient Approximation Made Simple. *Phys Rev Lett* **1996**, *77* (18), 3865. DOI: 10.1103/PhysRevLett.77.3865

(47) Momma, K.; Izumi, F. VESTA 3 for three-dimensional visualization of crystal, volumetric and morphology data. *J. Appl. Cryst.* **2011**, *44* (6), 1272–1276. DOI: 10.1107/S0021889811038970

(48) Rams, J.; Cabrera, J. M. Characterization of $LiNbO_3$ Waveguides Fabricated by Proton Exchange in Water. *Appl Phys A Mater Sci Process* **2005**, *81* (1), 205–208. DOI: 10.1007/s00339-004-2556-7

(49) Cai, L.; Wang, Y.; Hu, H. Low-Loss Waveguides in a Single-Crystal Lithium Niobate Thin Film. *Opt Lett* **2015**, *40* (13), 3013. DOI: 10.1364/ol.40.003013

(50) de Almeida, J. M. M. M. Design Methodology of Annealed H+ Waveguides in Ferroelectric $LiNbO_3$. *Optical Engineering* **2007**, *46* (6), 064601. DOI: 10.1117/1.2744364

(51) Xu, J.; Wang, C.; Tian, Y.; Wu, B.; Wang, S.; Zhang, H. Glass-on-$LiNbO_3$ Heterostructure Formed via a Two-Step Plasma Activated Low-Temperature Direct Bonding Method. *Appl Surf Sci* **2018**, *459*, 621–629. DOI: 10.1016/j.apsusc.2018.08.031

(52) Malovichko, G. I.; Grachev, V. G.; Kokanyan, E. P.; Schirmer, O. F.; Betzler, K.; Gather, B.; Jermann, F.; Klauer, S.; Schlarb, U.; Wöhlecke, M. Characterization of stoichiometric $LiNbO_3$ grown from melts containing K_2O. *Appl. Phys. A* **1993**, *56*, 103-108. DOI: 10.1007/BF00517674

(53) Schlarb, U.; Klauer, S.; Wesselmann, M.; Betzler, K.; Wöhlecke, M. Determination of the Li/Nb ratio in lithium niobate by means of birefringence and Raman measurements. *Appl. Phys. A* **1993**, *56*, 311-315. DOI: 10.1007/BF00324348

(54) Canali, C.; Carnera, A.; Della Mea, G.; Mazzoldi, P.; Al Shukri, S. M.; Nutt, A. C. G.; De La Rue, R. M. Structural Characterization of Proton Exchanged $LiNbO_3$ Optical Waveguides. *J Appl Phys* **1986**, *59* (8), 2643–2649. DOI: 10.1063/1.336968

(55) Cargo, J. T.; Filo, A. J.; Hughes, M. C.; Kannan, V. C.; Stevie, F. A.; Taylor, J. A.; Holmes, R. J. Characterization of Sulfuric Acid Proton-Exchanged Lithium Niobate. *J Appl Phys* **1990**, *67* (2), 627–633. DOI: 10.1063/1.345764

(56) Yu, M.; Zhao, L.; Wang, Y.; Xia, Y.; Ma, Y.; Wang, Y.; Han, X.; Chen, Y.; Lu, S.; Luo, G.; Zhu, N.; Yang, P.; Wang, K.; Lin, Q.; Jiang, Z. Plasma-Activated Silicon–Glass High-Strength Multistep Bonding for Low-Temperature Vacuum Packaging. *Chemical Engineering Journal* **2023**, *471*, 144719. DOI: 10.1016/j.cej.2023.144719

(57) Plach, T.; Hingerl, K.; Tollabimazraehno, S.; Hesser, G.; Dragoi, V.; Wimplinger, M. Mechanisms for Room Temperature Direct Wafer Bonding. *J Appl Phys* **2013**, *113* (9), 094905. DOI: 10.1063/1.4794319

(58) Rieutord, F.; Eymery, J.; Fournel, F.; Buttard, D.; Oeser, R.; Plantevin, O.; Moriceau, H.; Aspar, B. High-Energy x-Ray Reflectivity of Buried Interfaces Created by Wafer Bonding. *Phys Rev B Condens Matter Mater Phys* **2001**, *63* (12), 1254081–1254085. DOI: 10.1103/physrevb.63.125408

(59) Li, W.; Liang, T.; Chen, Y.; Jia, P.; Xiong, J.; Hong, Y.; Lei, C.; Yao, Z.; Qi, L.; Liu, W. Interface Characteristics of Sapphire Direct Bonding for High-Temperature Applications. *Sensors (Switzerland)* **2017**, *17* (9), 2080. DOI: 10.3390/s17092080

(60) Jiang, J.; Bitla, Y.; Huang, C. W.; Do, T. H.; Liu, H. J.; Hsieh, Y. H.; Ma, C. H.; Jang, C. Y.; Lai, Y. H.; Chiu, P. W.; Wu, W. W.; Chen, Y. C.; Zhou, Y. C.; Chu, Y. H. Flexible Ferroelectric Element Based on van Der Waals Heteroepitaxy. *Sci Adv* **2017**, *3* (6), e1700121. DOI: 10.1126/sciadv.1700121

(61) Wang, J.; Zhu, B.; Hao, Z.; Bo, F.; Wang, X.; Gao, F.; Li, Y.; Zhang, G.; Xu, J. Thermo-Optic Effects in on-Chip Lithium Niobate Microdisk Resonators. *Opt Express* **2016**, *24* (19), 21869. DOI: 10.1364/oe.24.021869

(62) Zhou, W. X.; Cheng, Y.; Chen, K. Q.; Xie, G.; Wang, T.; Zhang, G. Thermal Conductivity of Amorphous Materials. *Advanced Functional Materials* **2020**, *30* (8), 1903829. DOI: 10.1002/adfm.201903829

(63) Hewig, G. H.; Jain, K.; Sequeda, F. O.; Tom, R.; Wang, P.-W. R.F. Sputtering of $LiNbO_3$ thin films. *Thin Solid Films* **1982**, *88* (1), 67-74. DOI: 10.1016/0040-6090(82)90351-0

Table 1. Benchmark of Lithium niobate and Silicon direct bonding between this work and the previously reported methods.

Scheme	Environment	Annealing temperature (°C)	Bonding strength	Bonding interface	Damage to LN	Source
DWB	Air	200~500	Low	2 nm	None	19
SAB	Ultrahigh vacuum	Room temperature	High	6 nm	Yes	23,25
PAB	Air	Laser irradiation	Low	50 nm	Yes	21,22
PAB	Air	Room temperature	Low	NA	Yes	32,34
PAB	Air	150	Low	6.4 nm	Yes	31,35
LN: DWB; Si: PAB	Air	150	High	<2 nm	None	This work

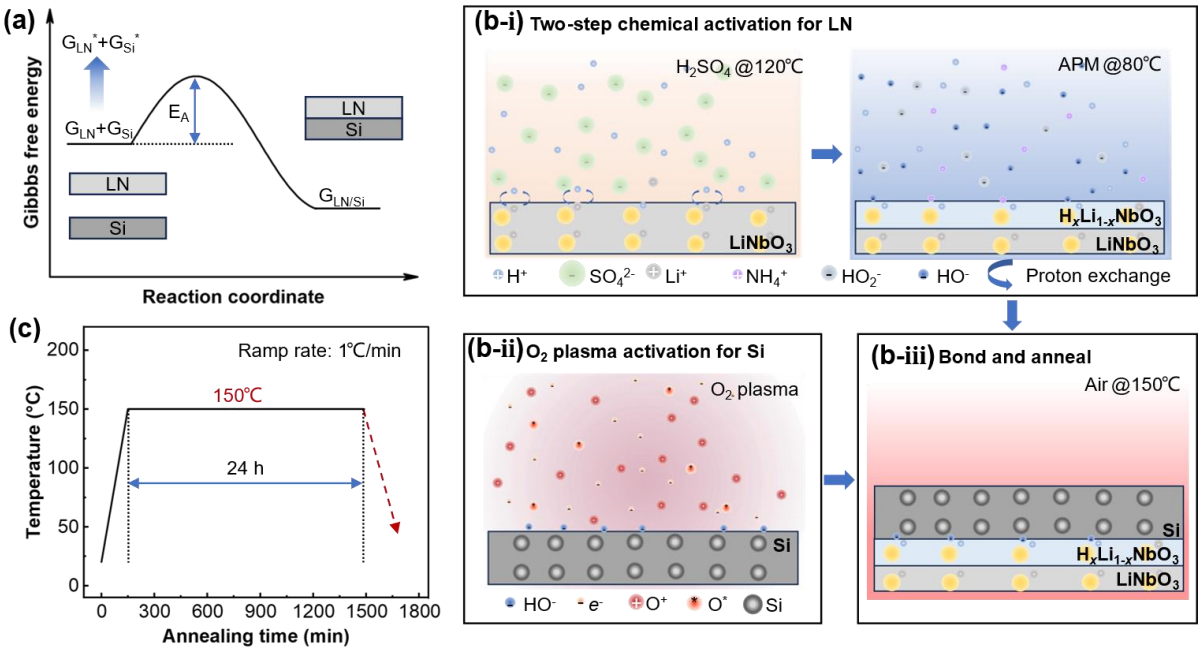

Figure 1. (a) Schematic bonding reaction; (b) Surface activation for (i) lithium niobate and (ii) silicon, (iii) bond and anneal; (c) Annealing curve at 150°C.

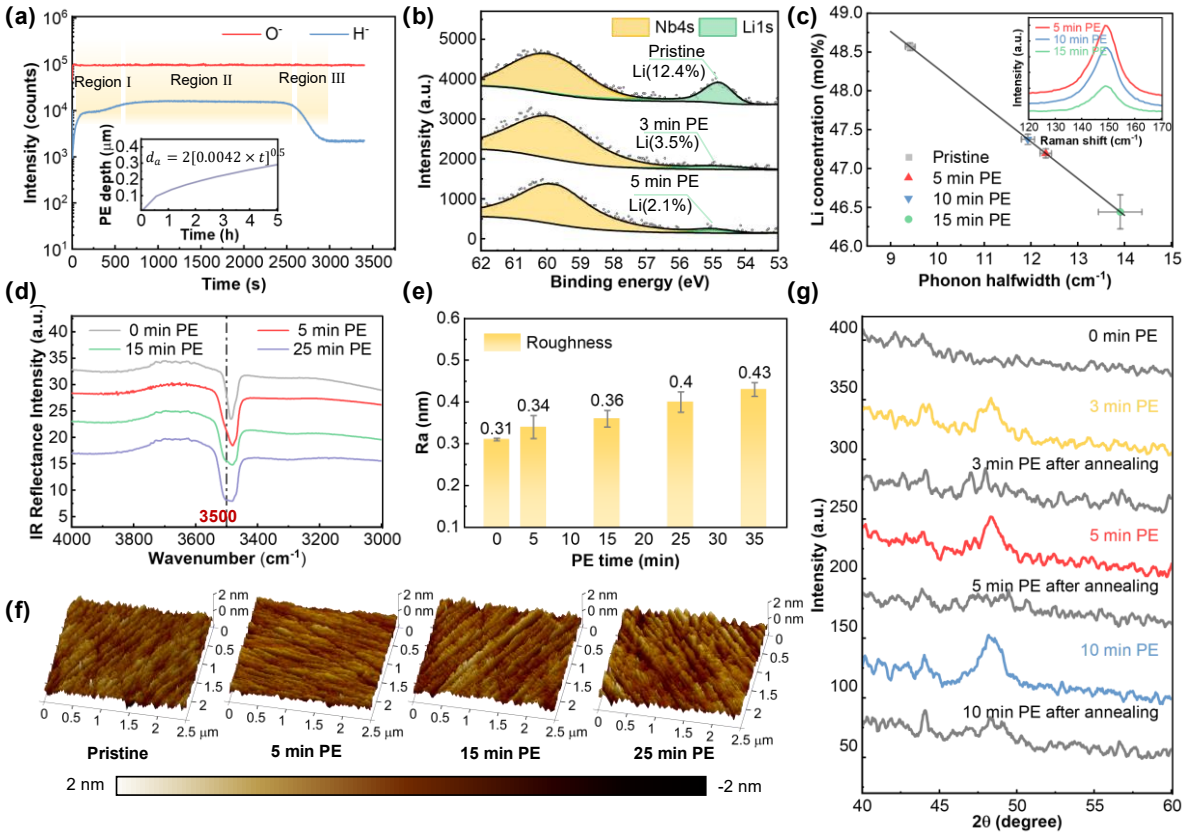

Figure 2. (a) SIMS signals on a LN crystal proton-exchanged for 2 hours (inserts in is the diffusion curve of sulfuric acid proton exchange at 120℃); (b) XPS spectra of Li1s after proton exchange of different time; (c) halfwidths of Raman lines at 153 cm^{-1} in LN versus Li content (inserts in is the Raman signals of LN with different periods PE); (d) FTIR absorbance, (e) roughness, (f) 3D morphology, and (g) GIXRD curves for LN after proton exchange of different time.

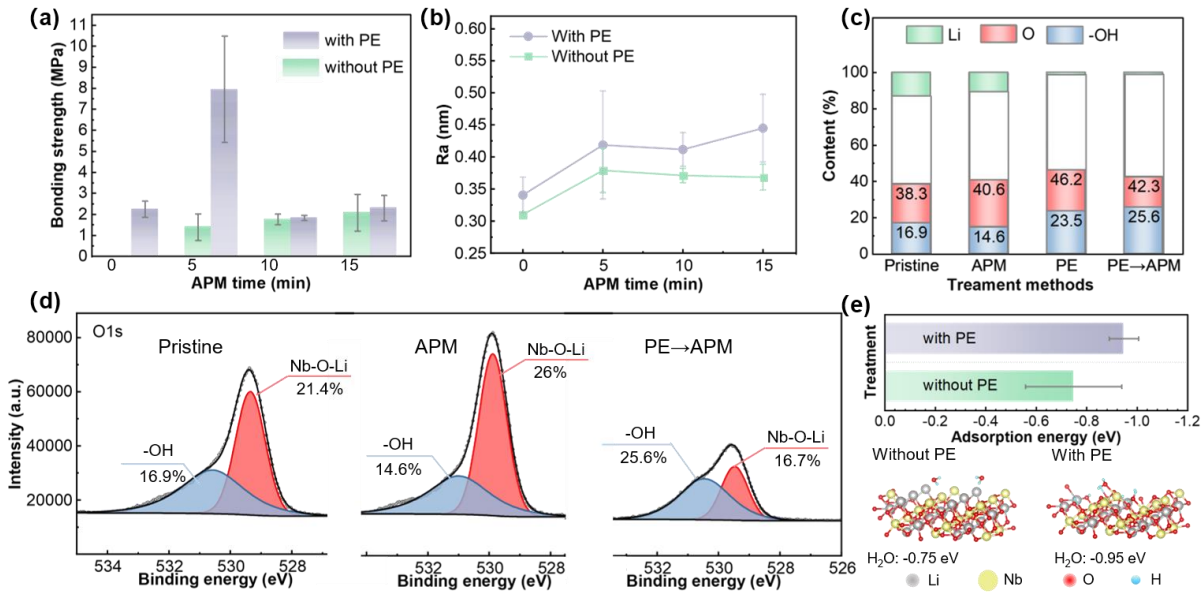

Figure 3. (a) Bonding strength and (b) roughness for LN and PELN followed by different periods APM; (c)functional groups contents, (d) XPS spectra of O1s and (e) adsorption energy of water for LN with and without PE.

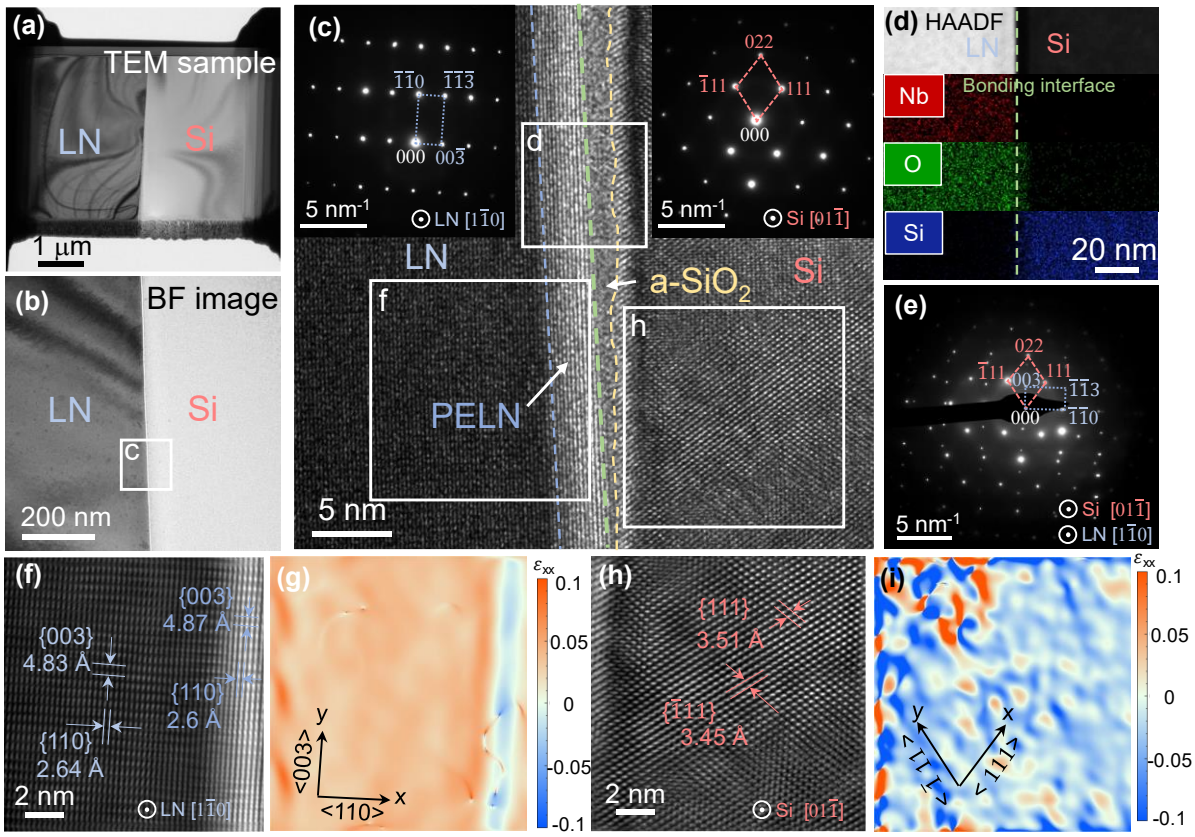

Figure 4. Cross-sectional TEM analysis for the bonding pair annealed at 150°C. (a) TEM sample by focused ion beam fabrication; (b) Bright-filed image and (c) high-resolution image of bonding interface (inserts in are the selected area diffraction spots); (d) HADDF image of the bonding interface and element mappings for Nb, O, and Si elements; (e) the selected area diffraction spots of the bonding interface; zoom-in view of the (f) LN and (h) Si side; the GPA strain profile results of the (g) LN and (i) Si side.

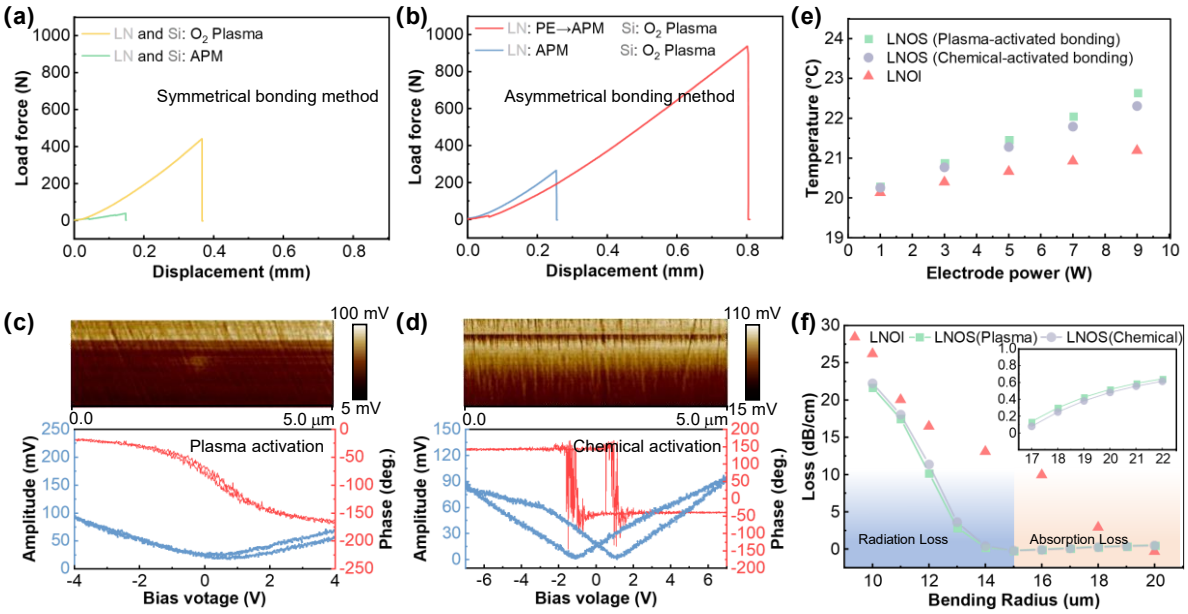

Figure 5. The tensile curves from (a) symmetrical and (b) asymmetrical bonding method; Representative local PFM amplitude and phase hysteresis loops on LN after (c) plasma activation and (d) chemical activation; (e) electrode power versus the waveguide temperature, and (f) bend losses versus the bend radius for LNOI, previous LNOS, and LNOS in this work.

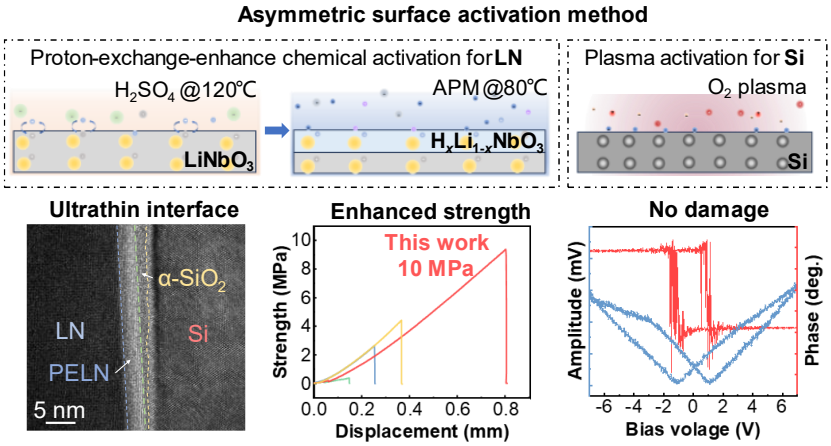

For Table of Contents Only